



Dynamics of Viscous Entrapped Saturated Zones in Partially Wetted Porous Media

Shuoqi Li¹ · Mingchao Liu^{1,2} · Dorian Hanaor³ · Yixiang Gan¹ 

Received: 19 February 2018 / Accepted: 27 June 2018 / Published online: 6 July 2018
© Springer Nature B.V. 2018

Abstract

As a typical multiphase fluid flow process, drainage in porous media is of fundamental interest both in nature and in industrial applications. During drainage processes in unsaturated soils and porous media in general, saturated regions, or clusters, in which a liquid phase fully occupies the pore space between solid grains, affect the relative permeability and effective stress of the system. Here, we experimentally study drainage processes in unsaturated granular media as a model porous system. The distribution of saturated clusters is analysed by optical imaging under different drainage conditions, with pore-scale information from Voronoi and Delaunay tessellation used to characterise the topology of saturated cluster distributions. By employing statistical analyses, we describe the observed spatial and temporal evolution of multiphase flow and fluid entrapment in granular media. Results indicate that the distributions of both the crystallised cell size and pore size are positively correlated to the spatial and temporal distribution of saturated cluster sizes. The saturated cluster size is found to follow a lognormal distribution, in which the generalised Bond number (Bo^*) correlates negatively to the scale parameter (μ) and positively to the shape parameter (σ). With further consideration of the total surface energy obtained based on liquid–air interfaces, we were able to include additional grain-scale information in the constitutive modelling of unsaturated soils using both the degree of saturation and generalised Bond number. These findings can be used to connect pore-scale behaviour with overall hydro-mechanical characteristics in granular systems.

Keywords Porous media · Multiphase fluid flow · Drainage process · Saturated cluster · Bond number

✉ Yixiang Gan
yixiang.gan@sydney.edu.au

¹ School of Civil Engineering, The University of Sydney, Sydney, Australia

² Department of Engineering Mechanics, CNMM & AML, Tsinghua University, Beijing 100084, China

³ Chair of Advanced Ceramic Materials, Technische Universität Berlin, Berlin, Germany

1 Introduction

Multiphase fluid flow in porous media is an important phenomenon with a broad range of applications, including risk assessment of landslides, biophysical systems and groundwater hydrology (Dai et al. 2002; Kueper and Frind 1988; Rahimi-Gorji et al. 2016; Saba and Illangasekare 2000; Seymour et al. 2004; Simmons et al. 1999). Predicting the properties of such systems usually requires pore-scale information including the topological features and interactions between intrinsic phases. In a multiphase flow system, as the wetting phase is withdrawn and replaced by the non-wetting phase (gas), the interface of wetting and non-wetting fluid phases tends to recede towards the outlet as a continuously moving front. The displacement dynamics of the interface mask the complex interplay of viscous, capillary and gravitational forces in the system (Aker et al. 2000; Bear and Braester 1972; Bryant and Blunt 1992; Lenormand and Zarcone 1985; Måløy et al. 1985; Savani et al. 2017; Schwarze et al. 2013; Youngs 1960).

Models used to study drainage processes in porous media include capillary tubes (Dullien et al. 1986; Morrow 1970; Youngs and Aggelides 1976) and two-dimensional Hele-Shaw cells (Haines 2009; Méheust et al. 2002). At high flow rates or in the absence of the stabilising effect of gravity, viscous forces tend to destabilise the continuous front, resulting in narrow fingers, which are the prerequisite condition for the generation of limited saturated zones behind the continuous front (Dullien et al. 1986; Måløy et al. 1985; Méheust et al. 2002; Morrow 1970; Youngs 1960; Youngs and Aggelides 1976). However, in previous studies viscous entrapped saturated zones left behind the moving front were neglected. Consequently, understanding interface dynamics between different liquids in drainage processes requires a better description of multiphase flow in porous media.

Fluid–fluid interface displacement in porous media along the front can be described at the pore scale as individual jumps at pore throats (Haines 2009; Lenormand and Zarcone 1989). Based on this, different approaches have been taken to explain the origin of fluid front morphologies, including a *coupled capillaries* model (Hoogland et al. 2015), which is established as a pair of neighbouring capillaries with different radii; a model consisting of small drops sliding down different substrates (Podgorski et al. 2001); and the use of sliding liquid elements (Su et al. 2004). The competition between viscous, capillary and gravitational forces during drainage in a two-dimensional synthetic porous medium was considered by Auradou et al. (1999) and Meheust et al. (2002) to deduce interface movements. For cases of two or more immiscible fluid phases in porous media, variations of the displacement structure are governed by the physical properties of the involved fluids and porous media (Meakin et al. 1986; Paterson 1984). These properties include the flow rates, wetting properties, viscosity ratio and density of the involved fluids, and the media's pore structure (Auradou et al. 1999; Podgorski et al. 2001; Su et al. 2004).

The formation of drainage fronts (i.e., the interfaces between wetting and non-wetting fluids) and displacement dynamics, shaped by the aforementioned properties, determine the residual liquid phase distribution in partially wetted porous media and affect the relative permeability of the correlated unsaturated regions (Auradou et al. 1999; Scherer et al. 2007). Recent experimental and numerical studies concerning drainage processes in porous media tend to focus mainly on the evolution of viscous fingering at various flow rates and flow velocity distributions along the continuous moving front (Alim et al. 2017; Holzner et al. 2015; Lenormand and Zarcone 1989; Matyka et al. 2016; Vishnudas and Chaudhuri 2017; Zhao et al. 2016). However, studies on the morphological characteristics of liquid phase entrapment behind the front remain relatively scarce. Accurate predictions of the fraction of liquid trapped behind the drainage front and its distribution are essential in order to quantify

the relative permeability and the effective stress of unsaturated soils and rocks (Blunt et al. 2002; Simmons et al. 1999).

For low flow rate conditions, fluid invasion events along the displacement front occur pore by pore and can be predicted by classic percolation theory (Gouyet et al. 1988; Hunt et al. 2014). However, for high flow rate cases, pores are invaded simultaneously, exhibiting large pressure bursts with liquid ejection. This phenomenon is manifested primarily through the complex interplay of three forces within the system, namely gravitational force, viscous force and capillary force (Or 2008). To quantify the contribution of these three forces to viscous unstable flows in porous media, two typical dimensionless parameters, i.e., Capillary number ($Ca = \eta v a^2 / \gamma k$) and Bond number ($Bo = \Delta \rho g' a^2 / \gamma$), are defined (Al-Fossail and Handy 1990; Alvarez et al. 2009; Birovljev et al. 1991; Blom and Hagoort 1998; Gawlinski and Stanley 1981; Méheust et al. 2002; Or 2008), where η is the viscosity of the wetting fluid, v the mean front velocity, γ the surface tension, and k the permeability of the porous medium, $\Delta \rho$ the density difference between the wetting and non-wetting fluids, g' the component of gravitational acceleration, and a is the typical pore size [more details can be found in Crisp and Williams (1971)]. It is clear that the Capillary number describes the ratio of viscous to capillary forces, while the Bond number indicates the ratio of gravitational to capillary forces. Following Méheust et al. (2002), these two dimensionless parameters can be combined as the generalised Bond number, $Bo^* = Bo - Ca$ (Méheust et al. 2002; Moebius and Or 2014), to quantify the transition between different flow regimes, i.e., stable and unstable flow. Specifically, positive values of Bo^* indicate stable moving fronts, while negative values of Bo^* mark unstable liquid fronts.

The flow rate dependency of the displacement front morphology raises the following question: how does the flow rate affect the liquid phase fraction trapped behind a moving drainage front? Wildenschild et al. (2005) used X-ray tomography to image air invasion into the saturated sandy soil and observed that large values of residual saturations occurred for high flow rates. The same trend was observed in glass bead micro-models in Løvvoll's study (Løvvoll et al. 2011). The observed increase in residual saturation behind the displacement front for higher flow rates occurs due to the preferential drainage of large pores bypassing and entrapping liquid phase in non-invaded volumes (Hoogland et al. 2015). It should be noted that liquid entrapment behind a rapidly moving front is not permanent, rather this liquid drains through a redistribution flow, albeit at a rate significantly lower than that of the primary moving front. This redistribution and the dominant liquid flow both affect the formation and evolution of these discontinuous entrapped liquid phases, which are termed locally saturated clusters. However, the extent and dynamics of locally saturated clusters are ripe for further exploration. An improved understanding of the behaviour drained and trapped liquid fractions in multiphase flow in porous media is of great value towards diverse engineering applications.

This study aims to establish a link between the complex mechanisms inside porous media and the morphological characteristics of a discontinuously entrapped liquid phase (i.e., saturated clusters). The properties of "viscous delayed" regions are studied in this work by establishing an experimental system where saturated clusters are obtained by the forced drainage of water from a porous medium. In this system, the gravitational and viscous forces can be tuned by changing tilting angles and drainage rates, and the competition of capillary, gravitational and viscous forces can be examined by introducing the generalised Bond number (Bo^*) to mark the onset of unstable flows. In the present paper, we describe an experimental set-up for the acquisition of entrapped liquid profiles and present data analysis methods to determine the influence of pore-scale structure on the spatial extent of saturated clusters and their size distributions under various drainage scenarios. Results

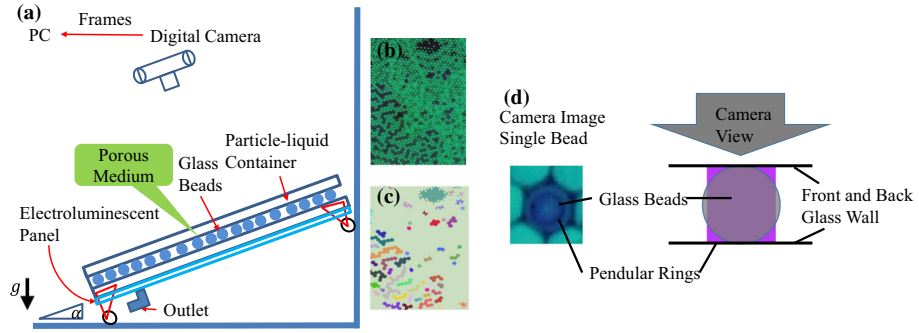


Fig. 1 Schematic illustration of the experimental set-up. **a** The camera, electroluminescent panel and cell are all connected to a common frame that can be tilted. The liquid outlet on the bottom is connected to a syringe pump that injects and withdraws the liquid. **b** A detailed zoomed-in section from the raw image extracted from the camera showing the structure of the porous network, the non-wetting phase (green) and wetting phase (dark red). **c** The same section after applying image processing. Individual saturated clusters are coloured randomly to allow the visualisation of separated clusters for different sizes. **d** Pendular rings between the glass bead and the front glass and schematic of a glass bead with pendular rings

are interpreted with a view towards their significance in partially saturated porous systems.

2 Methodology

2.1 Experimental Set-up

The present experimental system was designed for temporally and spatially resolved imaging interface motion in micro-models consisting of glass beads. The key elements of the set-up are shown in Fig. 1a. A micro-model was constructed by a single layer of glass beads with a diameter of 2 mm that were randomly arranged between two parallel glass plates. The plates and beads were then slightly compressed by clamps, and the model was sealed with silicone glue along the bottom and side edges, leaving the top side open to the atmosphere. The observable area was $180 \text{ mm} \times 270 \text{ mm}$, and the resulting porosity was about $n \approx 0.4$. After the model was installed, the outlet channel was connected to a high precision pump (Masterflex 77200-62, USA) to provide a stable volumetric injection and withdrawal flow rate. A digital camera (Nikon D3300) controlled by a computer over digiCamControl software was used to record the experiments at given time intervals based on different flow rates. Each image was rescaled to 1000×1500 pixels, which corresponds to a spatial resolution of 30 pixels 1 mm^2 (\sim the pore area). An electroluminescent panel provided sufficient background illumination for different shutter speeds. Both the digital camera and model could be tilted simultaneously to various inclination angles to control the gravitational component of the fluid flow in the porous medium. The component of gravity along the model g' is given by $g \sin(\alpha)$, where g is the gravitational acceleration and α is the inclination angle.

Water was used as the wetting fluid in all experiments, dyed with tracer (Cole-Parmer 00298-06, 2.6 ml/100 ml), and air was the non-wetting fluid invading from the open top edge. Experimental values of the wetting fluid were measured at $25 \text{ }^\circ\text{C}$. The surface tension between two fluids γ is 64.27 mN/m (std [standard deviation] = 0.15), which was performed by a goniometer (Rame-hart, model 200 Standard Contact Angle Goniometer with DROPim-

age Standard) using the pendent drop method. The wetting fluid has a dynamic viscosity η of 0.95 mPa.s (std = 0.2) and a density ρ of 998 kg/m³, whereas the non-wetting fluid has a dynamic viscosity η' of 1.84×10^{-2} mPa s and a density ρ' of 1.18 kg/m³. The permeability of the medium k was estimated from the Kozeny–Carman relation as 4.89×10^{-9} m² (Scheidegger 1958). The contact angle of water with the container wall is 44.56° (std = 0.18), which is a similar wettability to glass plates. The applied flow rates ranged from 1 to 20 ml/min for different tilt angles. These resulted in the mean front velocity determined from volumetric flow rates at the cross-sectional area taking into account the porosity, as shown in Table 1.

2.2 Image Processing

The grayscale pixel intensity histogram of raw images shows two distinguishable peaks corresponding to water and air phases. In order to separate the air-filled region from the saturated region, all grey levels under a given threshold were set to black ('wet'), while the others were white ('dry'). After thresholding, the whole observation area was separated into different regions with glass beads assigned to wet or dry regions. Here, only the saturated regions that are larger than the projection area of a typical glass bead (π mm² in this study) were considered. After removal of trapped liquid volumes with projection areas smaller than a single glass bead, the resulting black and white images provide the required geometrical information. To allow the visualisation of separate clusters of different sizes, analyses of morphological components were carried out and colours were assigned to the localised saturated clusters, as shown Fig. 1b, c. The inner rings in solid beads are shown in Fig. 1d. Small amounts of water are trapped in the void spaces between glass beads and the front and back walls. Based on the micro-model geometry, the pore space in our sample can be illustrated in two ways: a 3-D sphere network and a 2-D cylinder network. These entrapped liquid rings are discarded in this study.

To consider the influence of pore structures on saturated clusters, Voronoi and Delaunay meshes of the grain packing are generated from an individual image under saturated conditions, shown in Fig. 2. Figure 2a illustrates the algorithms for creating the two mesh types: solid red line-segments show the Delaunay triangulation, which is constructed on the basis of the distances between neighbouring beads, while blue dashed lines show the Voronoi lattice which identifies the set of points in the space which are closest to the centre of each cell. The top inset small images in Fig. 2b are zoomed-in cropped images from the Voronoi lattice. The colour map is used to display the values of void ratio (e) of individual cells. In Fig. 2b, e_{\max} has the value of 7.169 and e_{\min} is 0.103 as the theoretical limit for the hexagonal packing. The upper images in Fig. 2b show two typical crystallised and non-crystallised regions as parts of the larger lower image showing the overall experimental cell. This packing effect influences the resulting saturated cluster distribution. With the same aforementioned image processing methods, the centroids of glass beads are extracted, representing triangulation vertexes. Similar to the previous analysis for Fig. 2b, the largest void ratio for the Delaunay mesh is $e'_{\max} = 11.162$, while the smallest void ratio is $e'_{\min} = 0.103$, shown in Fig. 2c. In Fig. 2c, a pore is represented by the region inside each Delaunay triangle. To yield the void area, $\pi/2$ mm² is subtracted from the area of each triangle. In this manner, the Delaunay triangulation data can be transformed into a pore size distribution curve. Similarly, the Voronoi polygon area data stream can be transformed into cell-void size distribution curve.

Table 1 Evaluation of mean front velocity and generalised bond number (Bo^*) used for experiments

Tilt angle (°)	5					10					15				
	1	2	5	10	20	1	5	10	20	5	10	20	5	10	20
Drainage rate (ml/min)	0.116	0.231	0.579	1.157	2.315	0.116	0.579	1.157	2.315	0.579	2.315	2.315	0.579	2.315	2.315
Mean front velocity (mm/s)	0.116	0.231	0.579	1.157	2.315	0.116	0.579	1.157	2.315	0.579	2.315	2.315	0.579	2.315	2.315
Bo^* (-)	-1.556×10^{-4}	-3.111×10^{-4}	-7.778×10^{-4}	-0.002	-0.003	0.006	0.005	0.006	0.003	0.010	0.003	0.003	0.010	0.009	0.016

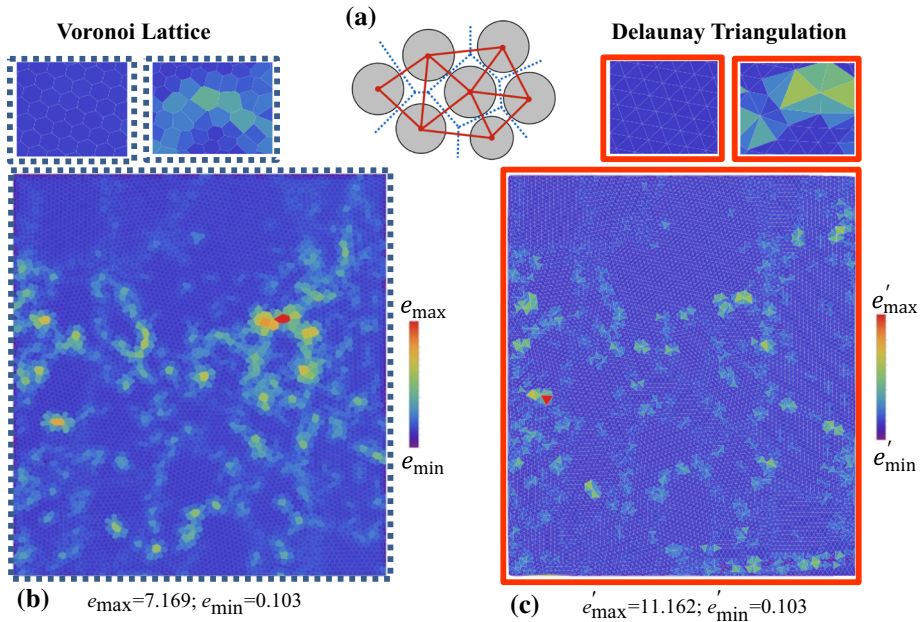


Fig. 2 a Schematics of Voronoi lattice (blue dashed lines) and Delaunay triangulation (red solid lines). **b** Map of Voronoi mesh for an individual fully saturated image. The bar legend is scaled in different gradient, ranging from smallest ($e_{\min} = 0.103$) to largest ($e_{\max} = 7.169$) Voronoi cell area. **c** Map of Delaunay mesh for an individual fully saturated image. The bar legend is scaled in different gradient, ranging from smallest ($e'_{\min} = 0.103$) to largest ($e'_{\max} = 11.162$) cell void ratio

2.3 Statistical Analysis

In this section, we use the probability density function (PDF), $f(y|w)$, specifying the data vector y under the given parameter w , which defines the shape of the distribution profile. Here, the subscript letter for the vector element y denotes statistically independent observations. According to the theory of probability, the PDF for $y = (y_1 \dots y_m)$ can be expressed as a multiplication of their PDFs. The probability density function of the lognormal distribution, which considers two parameters to describe the relative likelihood for the continuous random variable to take on a given value, is given as (Aitchison and Brown 1976)

$$f(X|\mu, \sigma^2) = \frac{1}{\sqrt{(2\pi\sigma^2)X}} \exp\left[-\frac{(\ln X - \mu)^2}{2\sigma^2}\right], \tag{1}$$

where the scale parameter μ is interpreted as the logarithmic mean of the random variables, and the shape parameter σ is interpreted as the standard deviation of the random variables in a logarithmic scale. As the parameters change in value, different probability distributions are generated. In this case, parameter estimation, a procedure of finding parameter values of a model that best fits the data, is vital to the following analysis.

In order to find the statistical parameters that best fit the acquired experimental dataset, the maximum likelihood estimation (MLE) method stands out for its attributes of sufficiency, consistency and efficiency (Myung 2003). By taking the product of the probability densities of the individual $X_i (i = 1, 2, 3, \dots, n)$, we derived the likelihood function of the lognormal

distribution for a series of X_i . The likelihood function $L(\mu, \sigma^2|X)$ is defined by reversing the roles of data vector and parameter vector: $L(\mu, \sigma^2|X) = \prod_{i=1}^n [f(X_i|\mu, \sigma^2)]$. By taking the natural logarithm of the likelihood function and taking the gradient of L with respect to μ and σ^2 while setting it equal to zero, we can find μ and σ^2 which maximise L (Ginos 2009). In addition, to measure the linear relationship between variables, the Pearson's correlation coefficient r is employed. Moreover, the correlation coefficient is a rescaled covariance: $r_{X,Y} = \frac{\text{cov}(X,Y)}{\sigma_X\sigma_Y}$, where $\text{cov}(X, Y)$ is the sample covariance, and σ_X and σ_Y are sample standard deviations. After rescaling the covariance, it ranges between -1 and +1, where 1 is total positive linear correlation, 0 is no linear correlation, and -1 is total negative linear correlation (Lee Rodgers and Nicewander 1988).

3 Results Analysis

3.1 Characterisation of Liquid Occupied Regimes

The flow of two immiscible fluids through a granular medium depends not only on the complex interplay between viscous, capillary and gravitational forces, but also the topological characteristics of the porous structure, here in particular the packing characteristics of the grains. The interaction between these forces and the pore structure yields a complex flow regime, shown in Fig. 3. It can be observed that there are four different liquid content forms, namely adsorbed, pendular, funicular and fully saturated regimes. The projection areas of these four regimes can be separated on the basis of their water content. In these four regimes, the water fraction increases from the top zoomed-in picture to the bottom one. Specifically, in the adsorbed regime, the liquid phase exists as a thin film coating on each sphere. As the liquid phase increases, pendular bridges form between adjacent spheres. When further water is added, the liquid phase becomes continuous, while the air phase becomes discontinuous, marking the funicular regime. Finally, in the fully saturated regime, all voids are occupied by the liquid phase. In the following sections, we focus on the spatial and temporal evolution of the fully saturated regime. Though the information from other regimes may be practically useful, e.g., the percolation of the liquid bridges presented in the pore space, their study may require higher resolution at the local scale.

3.2 Spatial Distribution of Wetted Cells

To look into the influence of packing characteristics on saturated cluster formation and evolution during drainage processes, the correlation between the temporal–spatial information of saturated clusters and packing characteristics is compared here. Figure 4 shows the spatial distributions of wetted cell density in two directions of the model for three flow conditions at two saturation levels. To remove boundary effects, the top edges of the model (about 20 grain diameters) are eliminated in our study. These spatial distributions are produced via a histogram of the data with linear binning of fully saturated Voronoi cells. All the points shown in Fig. 4 are the histogram heights with unit bin width. The wetted cells of interest in our analysis are those located inside saturated clusters.

In Fig. 4a, b, we divided the vertical span of the porous medium into 45 equal sub-windows with heights of 5 mm, spanning the entire width (230 mm). The histograms show the probability density of wetted cells within each sub-window along the y -coordinates, the distance between the sub-window centres and the outlet. These measurements are taken at

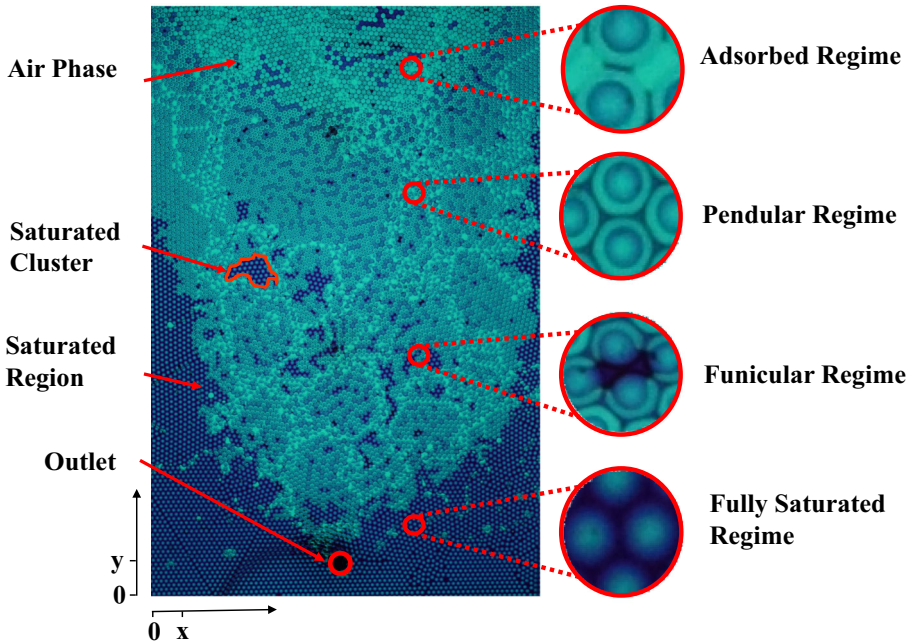


Fig. 3 An example experimental image revealing different saturation regimes

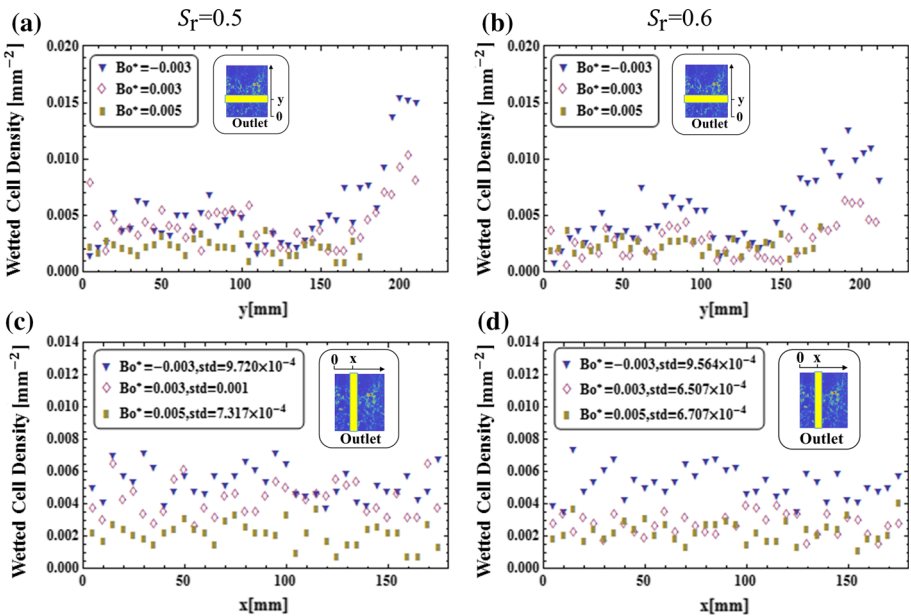


Fig. 4 Histogram showing the spatial distributions of wetted cells in the model for three experiments in a Voronoi mesh: **a**, **b** the wetted cell density inside sub-windows in the top–bottom direction for different saturation levels, as a function of the distance y to the outlet; **c**, **d** the wetted cell density in the perpendicular direction for different saturation levels. The insets show the corresponding sub-window orientations with respect to the model (made ≈ 4 times taller than the ones used in our analysis, to aid visualisation)

the time points when the liquid occupies 50% and 60% of the void space in the porous medium. Apart from the relatively large Voronoi cells randomly distributed along the model, the distributions are essentially constant for the most part of the system, with an increase for the sub-windows close to the top side of the system. However, experiments with relatively large generalised Bond numbers have a constant probability density of wetted cells along the top–bottom direction, which is reflected in the distribution points in Fig. 4a, b. The correlation observed between probability density differences arises from the fact that the generalised Bond number defines the stability of displacement structure. Additionally, as expected, the probability density of wetted cells tends to 0 for sub-windows close to the outlet, since the corresponding region filled with liquid phase and saturated clusters is only formed in the area mostly occupied by the air phase.

Similarly, in Fig. 4c, d we divided the horizontal span into 36 equal sub-windows, each having a width of 5 mm, and spanning the height of the studied medium (230 mm out the whole model height of 270 mm). The histograms show the probability density of wetted cells within sub-windows. To quantify the variance of our datasets, the standard deviation (std) is shown in the plot legends in Fig. 4c, d. The low standard deviation for each dataset indicates that the distribution is essentially stable, which shows that the boundaries on the x -axis of the model have little effect on the formation of saturated clusters. In addition, as can be seen, the mean values of the wetted cell probability density decrease as the generalised Bond number increases.

As can be seen in Fig. 4, the histograms in the first column ($S_r = 0.5$) show higher probability densities than those in the second column ($S_r = 0.6$) for the same sub-windows in both directions, i.e., the lower saturation level has more wetted cells than the high saturation level at the same region in the model. This is due to the removal of the large fully saturated region behind the liquid front, and for smaller saturation levels larger accumulated saturated areas can be extracted. This can be explained by considering that saturated clusters form when the liquid front meets different conductive pathways during drainage processes, and therefore, a sufficient distance along the flow direction is a prerequisite for the formation of such clusters. At lower saturation levels, a greater air content is present, more resistive pathways are bypassed, and subsequently, the accumulated area of viscous-detained liquid also increases. In addition, as Bo^* increases, the accumulated wetted cell area included in saturated clusters is reduced. This follows the aforementioned theory about the influence of Bo^* on geometry of liquid front in Sect. 2: for large negative values of Bo^* , the capillary fingers are widely spread along the liquid front during drainage processes; for large positive values of Bo^* , the liquid front is observed as a nearly flat geometry. For flat liquid fronts, gravity is always large enough to stabilise the displacement geometry leading to fewer saturated clusters trapped behind the liquid front and for unstable liquid fronts, more thin fingers can be observed, which are disconnected from the fully saturated region.

To look into the influence of packing characteristics on saturated cluster formation and evolution during drainage processes, we plot the number and probability distributions of wetted cells in Fig. 5. The wet cells are labelled with 1, and dry cells are labelled with 0. By collecting the amount of 1 labelled cells in an individual group divided by the number of cells in a group, the wetting probability for each group is computed. The details can be found in Appendix A. In Fig. 5, we specified the bin space as 0.4 mm^2 and collected a list of bins and histogram heights of the values. The pink curves with empty circles in each image are computed from initially fully saturated images with different drainage conditions. The other coloured curves represent wetted cell area distributions within saturated clusters for different saturation levels associated with different drainage conditions. For these cases, the largest continuous saturated region below the liquid front is removed

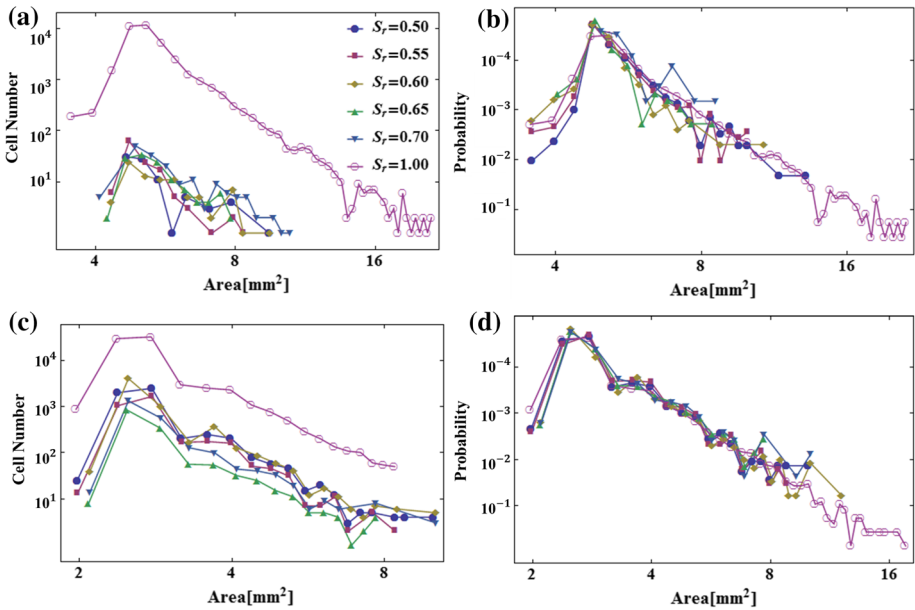


Fig. 5 Voronoi cell and Delaunay triangle area distributions for wetted regions (within saturated clusters) for six drainage conditions. The generalised Bond number in this case is -0.002 , which could be referred to the experiments in Table 1. The wetted cell number and probability distribution are calculated using Voronoi (a, b), and Delaunay tessellations (c, d)

from every picture and only saturated clusters were left behind in each frame. By employing image processing operations on individual images, we collected the data stream from five cases with the same flow conditions and merged all sub-lists as the final step. To have a better visualisation of how the data are distributed, we depicted both the wetted cell area number distribution and wetted cell area probability distribution as functions of cell area.

In Fig. 5a, b, it can be seen that the amount and frequency of Voronoi cells with areas in the range of 4–6 mm² are higher relative to cells with extremely small or large areas. By removing the projection area of individual glass beads (π mm² in this study), the void space in these cells is then found to be 1.72–5.72 mm³, which correlates to relatively close-packed regions in the experimental sample. Table 2 shows the pore-scale size parameters and wetting probabilities for Voronoi cells computed from five pictures. The experiment shown here corresponds to a saturation level value of 0.5 and a generalised Bond number of -0.003 . By grouping all cells with their individual face area, the corresponding dry/wet properties of every cell are also distributed into the same group. The relatively large values of wetting probability in Table 2 are most widely observed cells in the crystallised region. However, the smaller values are from cells with extremely large or small areas. This trend shows that the original cell size distribution of the porous medium can directly determine the probability distribution of wetted cell sizes for all cases, regardless of the total saturated area. Similarly, in Fig. 5c, d, results show that the probability distribution of the wetted cells perfectly follows the primary Delaunay cell size distribution.

Table 2 Pore-scale size parameters and wetted probabilities at different individual face area of Voronoi tessellation for $Bo^* = -0.003$, $S_r = 0.5$

Area of individual cell (mm ²)	Wetted probability (%)	Mean (mm ²)	Standard deviation (mm ²)
$Bo^* = -0.003$			
$3.14 < A < 4.14$	0.57	3.69	0.30
$4.14 \leq A < 5.14$	3.29	4.78	0.17
$5.14 \leq A < 6.14$	2.32	5.51	0.26
$6.14 \leq A < 7.14$	3.01	6.60	0.28
$7.14 \leq A < 8.14$	1.33	7.57	0.28
$8.14 \leq A < 9.14$	2.41	8.58	0.27
$9.14 \leq A < 10.14$	4.33	9.59	0.25
$10.14 \leq A < 11.14$	0.63	10.64	0.28

3.3 Saturated Cluster Distribution

To characterise the effect of drainage conditions on the evolution of saturated clusters, a statistical analysis of saturated cluster geometries was conducted. The largest saturated cluster identified in each image corresponds to the saturated region in front of the continuous liquid front and was therefore excluded from the analysis. Here, we first look at the effective size of the saturated clusters, which is acquired by collecting the number of pixels in a localised saturated region and dividing by the spatial resolution of 30 pixels per pore (1 mm²). To acquire sufficient data for statistical analysis, we performed five sets of experiments for each set of conditions. By grouping pictures with the same saturation, S_r , and generalised Bond number, Bo^* , and rearranging the experimental data into multiple sub-lists by a given bin size, the saturated cluster distributions are obtained.

The insert in Fig. 6a shows some observed elementary units of saturated clusters containing one to three glass beads during drainage processes. (I) In subfigure (1) in Fig. 6a, the central glass bead is fully coated and its neighbouring pores are occupied by the dyed liquid. In this subfigure, the saturated cluster is defined as the combination of the central glass bead and all its neighbouring pore spaces. (II) For saturated clusters with two glass beads inside, as shown in subfigure (2) in Fig. 6a, the volume of liquid in the inter-particle pore depends on the distance between two neighbouring beads, which can be quantified by considering the projection area of saturated clusters. (III) As for saturated clusters containing three beads, we assume that the pore structures in subfigure (3) in Fig. 6a are the same. However, owing to the fact that the capillary effect in granular media can be influenced by multiple factors, including pore size, flow rate and the gravitational force, the projection area of these two saturated clusters is different. These factors can be quantified by the generalised Bond number Bo^* . In what follows, saturated clusters are extracted for different values of S_r and Bo^* . By collecting all the data at each stage and plotting their probability density distribution, it is possible to determine appropriate distribution parameters that represent the dataset and relate these to Bo^* .

Figure 6b is a typical probability distribution of saturated cluster areas with liquid saturation level $S_r = 0.5$. After grouping the dataset with unit width bins equal to 2.5 mm², the dataset is separated into sub-lists, based on which the probability density distribution is calculated. It is observed that the probability density tends to the peak value (0.15–0.2/mm²)

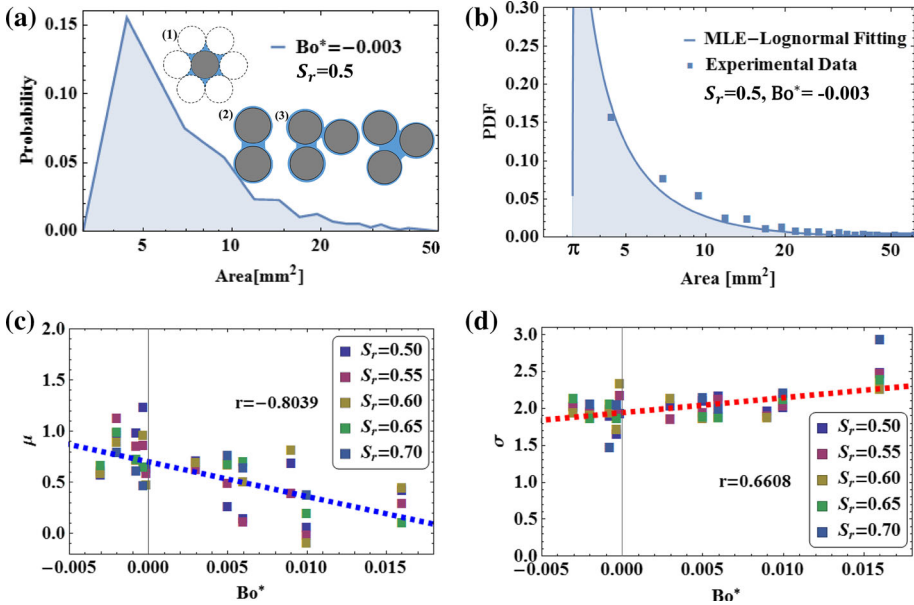


Fig. 6 **a** The size distribution of saturated clusters at a liquid saturation level of 0.5 with $Bo^* = -0.003$. **b** Saturated cluster distribution at the same degree of saturation ($S_r = 0.5$) with $Bo^* = -0.003$ (Dots: the experimental data, and Line: lognormal distribution by maximum likelihood estimation). **c** Scale parameter μ and **d** shape parameter σ as a function of generalised Bond number, Bo^* , for different saturation levels

around 4–8 mm². As can be seen in Fig. 5a, c, the distribution of wetted cell areas exhibits a peak for values around 4–8 mm², which corresponds to close-packed crystallised regions formed in the granular medium used here. Different types of distributions have also been tested, while a lognormal distribution function, Eq. (1), was selected here to best represent the experimental data. The goodness of fit for three common fitting models is further compared with details provided in Appendix B.

As stated in Sect. 2.3, the lognormal density distribution function has two parameters, namely the scale parameter μ and shape parameter σ , which govern the shape of the distribution curve. To estimate these two parameters from experimental observations, we use the maximum likelihood estimation (MLE) method, described in Sect. 2.3. The resulting lognormal distribution can then be plotted by substituting the specific parameters acquired from the MLE method, as in Fig. 6b. This figure illustrates the saturated cluster probability distribution as a function of area for different values of the generalised Bond number Bo^* at a specific saturation levels S_r , with good agreement found between the MLE-fitted distribution and experimental data. Due to the removal of saturated regions that are smaller than a projection area of a typical glass bead (π mm² in this study), the corresponding fitting curve in Fig. 6b starts at the point: $(\pi, 0)$.

After collecting parameters μ and σ for all series in the experiments, we evaluated Pearson’s correlation coefficient to quantify the relative linear relationship between them. To compute the correlation coefficient for both σ and μ as a function of Bo^* , we substitute the acquired values of these two parameters with respect to Bo^* into $r_{X,Y} = \frac{cov(X,Y)}{\sigma_X\sigma_Y}$. The correlated values for both parameters are shown in Fig. 6c, d. In Fig. 6c, the correlation coefficient of μ and Bo^* is -0.8039 , implying that all data points lay close to a line for

which μ decreases as Bo^* increases. On the contrary, the value of correlation coefficient of σ and Bo^* is 0.6608, indicating that σ increases as Bo^* increases, as shown in Fig. 6d.

For a given lognormal distribution, μ and σ are the mean and standard deviation of the variable's natural logarithm, respectively. The linear relations obtained for the lognormal density function parameters as functions of Bo^* are therefore correlated to the logarithmic mean and variation for saturated clusters sizes. In this case, as Bo^* increases, the logarithmic mean saturated cluster size decreases; meanwhile, the saturated cluster sizes tend slightly to spread out over a wider range of values. As stated in Sect. 1, in our experiments, Bo^* quantifies the complex interplay of viscous, capillary and gravitational forces in the porous medium. As a result, the correlations observed here with Bo^* show the saturated clusters are determined by the drainage conditions, with respect to the mean and standard deviation of the size distribution. This correlation can be used to predict the geometrical distributions of saturated clusters trapped behind a liquid front for known pore structures and drainage conditions.

4 Conclusion

In this study, we experimentally evaluated the formation of temporarily entrapped liquid phases in wetted granular materials and their subsequent evolution during drainage. In our experiments, the competition among viscous, gravitational and capillary forces was controlled to achieve different conditions of drainage from the porous media, which were characterised by the generalised Bond number, Bo^* . Due to the inhomogeneous capillary threshold (governed by pore throats) in the porous medium and dominance of viscous effects, saturated clusters were trapped behind the moving front. The spatial and temporal distribution of saturated clusters can thus be observed, and the following conclusions can be made:

1. The fraction of viscous limited pore bodies depends on the hydraulic properties of the resistive liquid phase, which is held in poorly connected pore clusters and small pore bodies due to the fact that the gravitational force cannot overcome the effect of the viscous force. It is demonstrated that, under various drainage conditions and saturation stages, the statistical distribution of the liquid phase is determined by the intrinsic pore network characteristics. It is found that the pore-scale structure has a strong influence on the spatial extent of viscous delayed pores during a multiphase flow. The wetted cell size probability curve closely follows the global-scale cell size probability curve.
2. The size of saturated clusters is found to follow a lognormal distribution, and the scale parameter μ and shape parameter σ negatively and positively correlate with Bo^* , respectively. Due to the fact that a relatively strong linear dependence exists between the lognormal distribution parameters, μ and σ , and generalised Bond number, Bo^* , we are thus able to describe cluster distribution for any given drainage conditions and saturation levels.

By extending the model to three-dimensional systems based on the explicit description of disordered pore networks, conclusions extracted from this study can be applied to a variety of situations in realistic geological scenarios involving multiphase flow. The ability to predict the presence of residual fluid phase left behind a moving liquid front on the basis of topological properties is of value in optimising water injection processes towards improved oil recovery (Blunt et al. 2002; Vishnudas and Chaudhuri 2017) and pollutant removal (Saba and Illangasekare 2000). The observations of the present study further show how particle scale

affects overall flow conditions, potentially facilitating improved formulation of the effective stress term in unsaturated soil mechanics (Likos 2014; Xu and Xie 2011).

The variation of the capillary threshold here was limited, due to the topological homogeneity inherent to packings of monosized glass beads. For more complex systems, a quantitative prediction of the viscous limited saturated cluster distribution remains challenging. The results presented here provide an initial step towards a better understanding of drainage in porous media, suggesting further detailed modelling and experimental studies into saturated clusters formation and evolution.

Acknowledgements The authors are grateful for the financial support from Australian Research Council (Projects DE130101639 and DP170102886) and The University of Sydney SOAR Fellowship.

Appendix A: Voronoi and Delaunay Tessellation Analysis

The procedures of using Voronoi and Delaunay tessellation in our statistical analysis are described in detail below:

1. We first compute Delaunay triangles and Voronoi cells associated with the network using the image processing method mentioned in Sect. 3. After numbering and collecting the vertex coordinates of every cell in both mesh regions, we are then able to create region-member functions associated with each cell, for instance, the i th region-member function for the i th cell.
2. We then import all pictures representing different saturation levels and drainage conditions into our calculation. These pictures are then be performed with morphological image processes and transformed into a black and white image, while the black and white pixels stand for dry and wetted regions, respectively. The black islands inside the white areas are the wetted clusters trapped during drainage. To focus on the saturated clusters behind the liquid front, we removed the largest continuous black island in each black and white picture, leaving other relatively small wetted clusters inside the pictures.
3. With the help of the built-in function (PixelValuePositions) in Mathematica, we then extracted all the positions of all black pixels in every picture. By repeatedly applying different black points into the i th region-member function, we extracted results of true or false for whether these points are region members of the i th cell. This step gave us the results of the amount of points in the i th cell, and we were then able to know the amount of black points in every cell by repeatedly employing this step on all remaining cells in individual pictures.
4. By comparing the ratio of black to white pixel counts, we classified the cells into two groups: dry and wet. After filtering the uncorrelated information from the aforementioned steps, we finally came to a list giving the area and wet (1)/dry (0) properties for every cell in an individual picture.

To enlarge our dataset, we repeated five experiments for each set of conditions and merged all five lists to perform further statistical analysis.

Appendix B: Goodness-of-Fit Test Results

Table 3 shows two widely used tests, the Pearson's χ^2 and *Anderson–Darling* methods to test the validity of three assumed distribution models (lognormal distribution, Weibull distribution

Table 3 Obtained maximum likelihood parameters from a specific dataset

$S_r = 0.5$ $Bo^* = -0.003$	Parameter		Pearson's χ^2		Anderson–Darling	
			Statistic	P value	Statistic	P value
Lognormal distribution	$\mu = 1.078$	$\sigma = 1.590$	23.841	0.690	0.582	0.665
Weibull distribution	$\alpha = 0.603$	$\beta = 6.538$	97.652	1.213×10^{-9}	11.755	3.019×10^{-4}
Gamma distribution	$\alpha = 0.463$	$\beta = 25.444$	202.537	2.267×10^{-9}	32.2891	0.000

Chi-square test and Anderson–Darling criterion are used to quantify the goodness of fit

and Gamma distribution). We applied a particular dataset ($S_r = 0.5$; $Bo^* = -0.003$) to the two test methods and listed the resulting values in Table 3. These results are used to verify the validity of lognormal distribution which has been selected on the basis of other prior considerations.

References

- Aitchison, J., Brown, J.A.C.: The Lognormal Distribution, vol. 5. CUP Archive, Cambridge (1976)
- Aker, E., Jørgen Måløy, K., Hansen, A.: Viscous stabilization of 2D drainage displacements with trapping. *Phys. Rev. Lett.* **84**(20), 4589–4592 (2000)
- Al-Fossail, K., Handy, L.L.: Correlation between capillary number and residual water saturation. *J. Colloid Interface Sci.* **134**(1), 256–263 (1990)
- Alim, K., Parsa, S., Weitz, D.A., Brenner, M.P.: Local pore size correlations determine flow distributions in porous media. *Phys. Rev. Lett.* **119**(14), 144501 (2017)
- Alvarez, N.J., Walker, L.M., Anna, S.L.: A non-gradient based algorithm for the determination of surface tension from a pendant drop: application to low Bond number drop shapes. *J. Colloid Interface Sci.* **333**(2), 557–562 (2009)
- Auradou, H., Måløy, K.J., Schmittbuhl, J., Hansen, A., Bideau, D.: Competition between correlated buoyancy and uncorrelated capillary effects during drainage. *Phys. Rev. E* **60**(6), 7224–7234 (1999)
- Bear, J., Braester, C.: On the flow of two immiscible fluids in fractured porous media. In: Iahr (ed.) *Developments in Soil Science*, pp. 177–202. Elsevier, Amsterdam (1972)
- Birovljev, A., Furuberg, L., Feder, J., Jssang, T., Mly, K.J., Aharony, A.: Gravity invasion percolation in two dimensions: experiment and simulation. *Phys. Rev. Lett.* **67**(5), 584–587 (1991)
- Blom, S.M.P., Hagoort, J.: How to Include the Capillary Number in Gas Condensate Relative Permeability Functions?. Society of Petroleum Engineers, New Orleans (1998)
- Blunt, M.J., Jackson, M.D., Piri, M., Valvatne, P.H.: Detailed physics, predictive capabilities and macroscopic consequences for pore-network models of multiphase flow. *Adv. Water Resour.* **25**(8–12), 1069–1089 (2002)
- Bryant, S., Blunt, M.: Prediction of relative permeability in simple porous media. *Phys. Rev. A* **46**(4), 2004–2011 (1992)
- Crisp, D.J., Williams, R.: Direct measurement of pore-size distribution on artificial and natural deposits and prediction of pore space accessible to interstitial organisms. *Mar. Biol.* **10**(3), 214–226 (1971)
- Dai, F.C., Lee, C.F., Ngai, Y.Y.: Landslide risk assessment and management: an overview. *Eng. Geol.* **64**(1), 65–87 (2002)
- Dullien, F.A.L., Lai, F.S.Y., MacDonald, I.F.: Hydraulic continuity of residual wetting phase in porous media. *J. Colloid Interface Sci.* **109**(1), 201–218 (1986)
- Gawlinski, E.T., Stanley, H.E.: Continuum percolation in two dimensions: Monte Carlo tests of scaling and universality for non-interacting discs. *J. Phys. A: Math. Gen.* **14**(8), L291 (1981)
- Ginos, B.F.: Parameter estimation for the lognormal distribution [M.S. thesis]. Brigham Young University, Provo, Utah (2009).
- Gouyet, J., Rosso, M., Sapoval, B.: Fractal structure of diffusion and invasion fronts in three-dimensional lattices through the gradient percolation approach. *Phys. Rev. B: Condens. Matter* **37**(4), 1832 (1988)

- Haines, W.B.: Studies in the physical properties of soil. V. The hysteresis effect in capillary properties, and the modes of moisture distribution associated therewith. *J. Agric. Sci.* **20**(1), 97–116 (2009)
- Holzner, M., Morales, V.L., Willmann, M., Dentz, M.: Intermittent Lagrangian velocities and accelerations in three-dimensional porous medium flow. *Phys. Rev. E* **92**(1), 013015 (2015)
- Hoogland, F., Lehmann, P., Or, D.: The formation of viscous limited saturation zones behind rapid drainage fronts in porous media. *Water Resour. Res.* **51**(12), 9862–9890 (2015)
- Hunt, A., Ewing, R., Ghanbarian, B.: *Percolation Theory for Flow in Porous Media*, vol. 880. Springer, Berlin (2014)
- Kueper, B.H., Frind, E.O.: An overview of immiscible fingering in porous media. *J. Contam. Hydrol.* **2**(2), 95–110 (1988)
- Lee Rodgers, J., Nicewander, W.A.: Thirteen ways to look at the correlation coefficient. *Am. Stat.* **42**(1), 59–66 (1988)
- Lenormand, R., Zarcone, C.: Invasion percolation in an etched network: measurement of a fractal dimension. *Phys. Rev. Lett.* **54**(20), 2226–2229 (1985)
- Lenormand, R., Zarcone, C.: Capillary fingering: percolation and fractal dimension. *Transp. Porous Media* **4**(6), 599–612 (1989)
- Likos, W.J.: Effective stress in unsaturated soil: accounting for surface tension and interfacial area. *Vadose Zone J.* (2014). <https://doi.org/10.2136/vzj2013.05.0095>
- Løvøll, G., Jankov, M., Måløy, K.J., Toussaint, R., Schmittbuhl, J., Schäfer, G., Méheust, Y.: Influence of viscous fingering on dynamic saturation-pressure curves in porous media. *Transp. Porous Media* **86**(1), 305–324 (2011)
- Måløy, K.J., Feder, J., Jøssang, T.: Viscous fingering fractals in porous media. *Phys. Rev. Lett.* **55**(24), 2688–2691 (1985)
- Matyka, M., Golembiewski, J., Koza, Z.: Power-exponential velocity distributions in disordered porous media. *Phys. Rev. E* **93**(1), 013110 (2016)
- Meakin, P., Coniglio, A., Stanley, H.E., Witten, T.A.: Scaling properties for the surfaces of fractal and nonfractal objects: an infinite hierarchy of critical exponents. *Phys. Rev. A* **34**(4), 3325–3340 (1986)
- Méheust, Y., Løvøll, G., Måløy, K.J., Schmittbuhl, J.: Interface scaling in a two-dimensional porous medium under combined viscous, gravity, and capillary effects. *Phys. Rev. E* **66**(5), 051603 (2002)
- Moebius, F., Or, D.: Pore scale dynamics underlying the motion of drainage fronts in porous media. *Water Resour. Res.* **50**(11), 8441–8457 (2014)
- Morrow, N.R.: Irreducible wetting-phase saturations in porous media. *Chem. Eng. Sci.* **25**(11), 1799–1815 (1970)
- Myung, I.J.: Tutorial on maximum likelihood estimation. *J. Math. Psychol.* **47**(1), 90–100 (2003)
- Or, D.: Scaling of capillary, gravity and viscous forces affecting flow morphology in unsaturated porous media. *Adv. Water Resour.* **31**(9), 1129–1136 (2008)
- Paterson, L.: Diffusion-limited aggregation and two-fluid displacements in porous media. *Phys. Rev. Lett.* **52**(18), 1621–1624 (1984)
- Podgorski, T., Flesselles, J.M., Limat, L.: Corners, cusps, and pearls in running drops. *Phys. Rev. Lett.* **87**(3), 036102 (2001)
- Rahimi-Gorji, M., Gorji, T.B., Gorji-Bandpy, M.: Details of regional particle deposition and airflow structures in a realistic model of human tracheobronchial airways: two-phase flow simulation. *Comput. Biol. Med.* **74**, 1–17 (2016)
- Saba, T., Illangasekare, T.H.: Effect of groundwater flow dimensionality on mass transfer from entrapped nonaqueous phase liquid contaminants. *Water Resour. Res.* **36**(4), 971–979 (2000)
- Savani, I., Sinha, S., Hansen, A., Bedeaux, D., Kjelstrup, S., Vassvik, M.: A Monte Carlo algorithm for immiscible two-phase flow in porous media. *Transp. Porous Media* **116**(2), 869–888 (2017)
- Scheidegger, A.E.: The physics of flow through porous media. *Soil Sci.* **86**(6), 355 (1958)
- Scherer, G.W., Valenza II, J.J., Simmons, G.: New methods to measure liquid permeability in porous materials. *Cem. Concr. Res.* **37**(3), 386–397 (2007)
- Schwarze, R., Gladky, A., Uhlig, F., Luding, S.: Rheology of weakly wetted granular materials: a comparison of experimental and numerical data. *Granul. Matter* **15**(4), 455–465 (2013)
- Seymour, J.D., Gage, J.P., Codd, S.L., Gerlach, R.: Anomalous fluid transport in porous media induced by biofilm growth. *Phys. Rev. Lett.* **93**(19), 198103 (2004)
- Simmons, C.T., Narayan, K.A., Wooding, R.A.: On a test case for density-dependent groundwater flow and solute transport models: the Salt Lake Problem. *Water Resour. Res.* **35**(12), 3607–3620 (1999)
- Su, G.W., Geller, J.T., Hunt, J.R., Pruess, K.: Small-scale features of gravity-driven flow in unsaturated fractures. *Vadose Zone J.* **3**, 592–601 (2004)
- Vishnudass, R., Chaudhuri, A.: A comprehensive numerical study of immiscible and miscible viscous fingers during chemical enhanced oil recovery. *Fuel* **194**, 480–490 (2017)

- Wildenschild, D., Hopmans, J., Rivers, M., Kent, A.: Quantitative analysis of flow processes in a sand using synchrotron-based X-ray microtomography. *Vadose Zone J.* **4**(1), 112–126 (2005)
- Xu, H., Xie, K.: Effective stress in soils under different saturation conditions. *J. Cent. South Univ. Technol.* **18**(6), 2137–2142 (2011)
- Youngs, E.G.: The drainage of liquids from porous materials. *J. Geophys. Res.* **65**(12), 4025–4030 (1960)
- Youngs, E.G., Aggelides, S.: Drainage to a water table analysed by the Green-Ampt approach. *J. Hydrol.* **31**(1–2), 67–79 (1976)
- Zhao, B., MacMinn, C.W., Juanes, R.: Wettability control on multiphase flow in patterned microfluidics. *Proc. Natl. Acad. Sci.* **113**(37), 10251–10256 (2016)